Intracavity signal amplification system for next-generation gravitational-wave detectors

K. Somiya,* K. Suzuki, S. Otabe, and K. Harada

Graduate School of Science and Technology, Tokyo Institute of Technology, Meguro-ku, Tokyo 152-8551, Japan

(Received 3 February 2023; accepted 5 June 2023; published 27 June 2023)

This article summarizes our study to develop an intracavity parametric signal amplification system for improving the sensitivity of a gravitational-wave detector at high frequencies to aim at an observation of a postmerger remnant of a binary neutron star collision. The detector configuration is based on a dual recycling interferometer and an optical parametric amplifier crystal is inserted into the signal recycling cavity. The cavity is detuned and an optical spring is generated for the differential motion of the two end mirrors. The amplifier converts the energy of the pump beam to the optical spring and the spring frequency can be enhanced to a few kilohertz. The system is contrasting to the squeeze injection technique commonly used in second-generation gravitational-wave detectors. Although both techniques use an optical parametric amplifier crystal, the squeeze injection reduces noise while signal amplification increases the signal to modify the optomechanical dynamics of the system.

DOI: 10.1103/PhysRevD.107.122005

I. GRAVITATIONAL WAVES AT kHz

Since the great discovery of gravitational waves by LIGO in 2015 [1], nearly a hundred events have been observed in the global gravitational-wave detectors network. The observation band of the currently operating detectors, which is defined with the strain sensitivity better than $10^{-23}(1/\sqrt{\mathrm{Hz}})$, is from a few tens of Hertz to 1–2 kHz. The band is slightly lower than the expected merger frequency of neutron star binaries. Although several neutron star binary inspirals have been observed by LIGO and Virgo [2], a clear footprint of the merger and postmerger signal has not been obtained. Several models exist to explain the equation of state of a neutron star and the observation of the gravitational wave at the merger is said to be the only way to acquire information about mysterious astronomical object [3].

Several proposals have been made to observe high-frequency gravitational waves. NEMO is a new detector planned to be built in Australia [4]. It employs silicon mirrors cooled down to 123–150 K to take advantage of the low thermal lensing effect due to the high thermal conductivity of the material, and make the most use of the low thermal expansion at 123 K to reduce the thermoelastic dissipation. KAGRA+ is an upgrade plan of KAGRA, the currently operating detector in Japan [5]. One of the proposals states that thicker and shorter sapphire suspension fibers are employed to extract more heat to allow a few megawatts of light in the arm cavities [6]. Both NEMO and KAGRA+ aim to start the operation between second- and third-generation detectors (Einstein Telescope [7] and Cosmic Explorer [8]).

The limiting noise source at such high frequencies is the quantum shot noise. The signal extraction port of the laser interferometric detector is kept at the dark fringe. The vacuum field that enters the interferometer from its dark port is the source of the shot noise [9]. The substitution of the vacuum field by the field squeezed in the phase quadrature reduces the shot noise level. The squeeze injection technique has already been implemented in most of the currently operating detectors [10–12]. Tuning the interferometer's resonant condition to increase the signal response is another way to improve shot noise. A typical cavity bandwidth is narrower than that of the kilohertz. A slight detuning of the cavity helps shift the resonance from the laser frequency to the kilohertz signal sideband frequency [13]. Even without detuning, the phase rotation inside the interferometer helps shift the resonant condition if the signal recycling cavity (SRC) at the interferometer's dark port is long; this phase rotation is called the long-SRC effect [14]. NEMO, and perhaps KAGRA+, plan to employ the long-SRC configuration. The detuning of the SRC converts a part of the phase modulation signal sideband to the amplitude modulation that couples with the laser to generate a radiation pressure force on the mirror. The optomechanical loop creates an optical spring [15]. Analogous to a bar-type detector, the gravitational wave signal is enhanced at the resonance of the optical spring. It would be an alternative candidate to improve the sensitivity at high frequencies with the optical spring frequency possibly increasing to a few kilohertz.

*somiya@phys.titech.ac.jp

Adding an active filter inside the SRC is a breakthrough to circumvent the so-called Mizuno limit, which explains the trade-off between the peak sensitivity and bandwidth with a given laser power [16]. The basic idea of the intracavity active filter can be found in intracavity readout schemes [17], particularly in the optical lever scheme proposed by Khalili [18]. Chen revisited the optical lever and invented an intracavity ponderomotive amplifier [19]. The ponderomotive amplifier comprises an auxiliary interferometer with light mirrors connected to the dark port of the main interferometer. The phase signal from the main interferometer is coupled with the laser light of the auxiliary interferometer to generate radiation pressure on the light mirrors. The phase signal from the auxiliary interferometer is sent to the main interferometer. The external energy of the laser in the auxiliary interferometer is introduced to actively amplify the signal. By replacing the ponderomotive amplifier with an optical parametric amplifier, Somiya proposed an intracavity parametric signal amplification system first without SRC detuning [20] and then with SRC detuning [21]. Further advanced versions of the intracavity schemes have been proposed since then. Adya proposed an intracavity squeezing with the long-SRC effect [22]. Korobko combined a nondetuned parametric amplifier with the long-SRC effect to effectively enhance the bandwidth of an interferometer (quantum expander) [23]. Miao invented a scheme to use the negative dispersion of a micro-resonator to expand the cavity bandwidth (white-light cavity) [24–27].

In this article, we summarize our study on the parametric signal amplification system. In our previous work [21], the interferometer configuration was a resonant sideband extraction that comprises a Michelson interferometer with a Fabry-Perot resonator in each arm and two recycling cavities. We have found that a dual recycling interferometer without arm resonators is more suitable for the amplification system because the amplifier in SRC decreases the bandwidth. (An alternative approach would be to use two signal recycling mirrors as is suggested, for example, by Miao [28].) This is the configuration of the existing gravitational-wave detector GEO600 [29]. We assume an arm length of GEO600 ($L = 1200$ m) and anticipate implementing the signal amplification system in GEO600 in the near future. This article will answer some unanswered questions about intracavity system: (i) why the detune angle needs to be around $\pi/4$ and (ii) why the intracavity system is sensitive to the optical loss in the interferometer. The optical losses and squeeze angle rotation, which were not included in our previous work [21], are introduced. In Sec. II, we provide a mathematical expression for the response of the dual-recycling interferometer without losses and discuss the optical resonance and optical spring frequencies with parametric amplification. In Sec. III, we calculate the sensitivity spectrum and discuss the condition to improve the signal-to-noise ratio with different parameter sets. In Sec. IV, we discuss the optical losses and we present our target sensitivity curve in Sec. V.

II. INPUT-OUTPUT RELATION OF THE INTERFEROMETER WITH THE INTRACAVITY AMPLIFIER

Figure 1 illustrates our setup. The laser light at ω_0 is injected into the interferometer and serves as the carrier light to probe the displacement of the mirrors. The electromagnetic field around the carrier light at time t in the Heisenberg picture is given by

$$E(t) = \sqrt{\frac{2\pi\hbar\omega_0}{\mathcal{A}c}} e^{-i\omega_0 t} \int_0^\infty [a_+ e^{-i\Omega t} + a_- e^{i\Omega t}] \frac{d\Omega}{2\pi} + \text{H.c.}, \tag{1}$$

where $a_\pm$ is the annihilation operator at $\omega_0 \pm \Omega$, $\mathcal{A}$ is the cross sectional area of the beam, and H.c. means the Hermitian conjugate. It is common to use the two-photon formalism [30] to express the amplitude and phase quadrature components of the carrier light: $a_1 = (a_+ + a_-)/\sqrt{2}, a_2 = (a_+ - a_-)/\sqrt{2}i$. Bold letters in Fig. 1 are vectors with the amplitude quadrature component (subscript "1") in the top column and the phase quadrature component (subscript "2") in the bottom column. These fields satisfy the commutation relations: $[a_1(\Omega), a_2^\dagger(\Omega')] = -[a_2(\Omega), a_1^\dagger(\Omega')] = 2\pi i\delta(\Omega - \Omega')$. The interferometer is operated at the dark fringe such that all the light field entering from the laser is reflected to the laser source. The output field to the photodetector comes from the interferometer's dark port. The input-output relations of the fields are given as

$$\begin{aligned} &\boldsymbol{b} = -r_s\boldsymbol{a} + t_s\boldsymbol{f}, \qquad \boldsymbol{e} = r_s\boldsymbol{f} + t_s\boldsymbol{a}, \qquad \boldsymbol{c} = \mathbb{R}(\phi)\boldsymbol{e}, \\ &\boldsymbol{f} = \mathbb{R}(\phi)\mathbb{S}(s,\eta)\boldsymbol{d}, \qquad \boldsymbol{d} = \mathbb{K}\boldsymbol{c}e^{2i\beta} + \alpha\boldsymbol{h}e^{i\beta}. \end{aligned} \tag{2}$$

Here r_s and t_s are the amplitude reflectivity and transmittance of the signal recycling mirror, $\beta = L\Omega/c$ is the phase delay of the signal field after a single trip of the arm with L as the arm length and c as the light speed, $\alpha = \sqrt{2\omega_0 I_{\rm BS} L^2/(\hbar c^2)}$ represents the signal strength with $I_{\rm BS}$ the laser power at the beam splitter and $\hbar$ the Planck's constant, $\boldsymbol{h} = (0, h)^T$ with h the gravitational-wave signal in strain, and $\mathbb{R}(\phi)$ is the rotation matrix with ϕ as the detune phase of the SRC. $\mathbb{S}(s,\eta)$ is the squeezing matrix with a squeeze factor s and squeeze angle η and $\mathbb{K}$ is the optomechanical coupling matrix of the interferometer, which are given as follows:

$$\mathbb{S}(s,\eta) = \mathbb{R}(\eta)\begin{pmatrix} s & 0 \\ 0 & 1/s \end{pmatrix}\mathbb{R}(-\eta), \tag{3}$$

$$\mathbb{K} = \begin{pmatrix} 1 & 0 \\ -\mathcal{K} & 1 \end{pmatrix}, \qquad \mathcal{K} = \frac{4\omega_0 I_{\rm BS}}{mc^2\Omega^2}. \tag{4}$$

Note that the squeezing matrix is operated to the field propagating downstream from the beam splitter to the signal recycling mirror as the pump beam is injected to the crystal in the direction. The location of the crystal inside the SRC is unspecified. Equation (3) demonstrates that the phase rotation of the field before entering the crystal can be included in the squeeze angle rotation η. Solving the series of Eqs. (2)–(4), we obtain the input-output relation of the interferometer:

$$\boldsymbol{b} = \frac{1}{M}(\mathbb{A}\boldsymbol{a}e^{2i\beta} + \mathbb{H}\boldsymbol{h}e^{i\beta}) \tag{5}$$

with

$$\begin{aligned}
M &= s + sr_s^2 e^{4i\beta} - r_s e^{2i\beta}\Big[(1+s^2)\cos 2\phi \\
&\quad + \frac{\mathcal{K}}{2}\{(1+s^2)\sin 2\phi + (1-s^2)\sin(2\phi+2\eta)\}\Big], \\
A_{11} &= \frac{1+s^2}{2}(1+r_s^2)\cos 2\phi - \frac{1-s^2}{2}t_s^2\cos 2\eta \\
&\quad + \frac{\mathcal{K}}{4}[(1+r_s^2)(1+s^2)\sin 2\phi + t_s^2(1-s^2)\sin 2\eta \\
&\quad + (1+r_s^2)(1-s^2)\sin(2\phi+2\eta)] - 2sr_s\cos 2\beta, \\
A_{12} &= -\frac{t_s^2}{2}\Big[(1+s^2)\sin 2\phi + (1-s^2)\sin 2\eta \\
&\quad + \frac{\mathcal{K}}{2}\{2(1+s^2)\sin^2\phi + (1-s^2)\cos 2\eta \\
&\quad - (1-s^2)\cos(2\phi+2\eta)\}\Big], \\
A_{21} &= \frac{t_s^2}{2}\Big[(1+s^2)\sin 2\phi - (1-s^2)\sin 2\eta \\
&\quad - \frac{\mathcal{K}}{2}\{2(1+s^2)\cos^2\phi + (1-s^2)\cos 2\eta \\
&\quad + (1-s^2)\cos(2\phi+2\eta)\}\Big], \\
A_{22} &= \frac{1+s^2}{2}(1+r_s^2)\cos 2\phi + \frac{1-s^2}{2}t_s^2\cos 2\eta \\
&\quad + \frac{\mathcal{K}}{4}[(1+r_s^2)(1+s^2)\sin 2\phi - t_s^2(1-s^2)\sin 2\eta \\
&\quad + (1+r_s^2)(1-s^2)\sin(2\phi+2\eta)] - 2sr_s\cos 2\beta, \\
H_{12} &= -\frac{t_s\alpha}{2}[(1+s^2+2sr_s e^{2i\beta})\sin\phi \\
&\quad + (1-s^2)\sin(\phi+2\eta)], \\
H_{22} &= \frac{t_s\alpha}{2}[(1+s^2-2sr_s e^{2i\beta})\cos\phi \\
&\quad + (1-s^2)\cos(\phi+2\eta)], \\
H_{11} &= H_{21} = 0.
\end{aligned} \tag{6}$$

By selecting the readout phase ζ, given by the relative phase of a local oscillator to the amplitude quadrature, we observe the output field $b_\zeta = b_1\cos\zeta + b_2\sin\zeta$. The signal response function is given by $|(H_{12}\cos\zeta + H_{22}\sin\zeta)/M|$, the noise response function is given by

$$\frac{\sqrt{|A_{11}\cos\zeta + A_{21}\sin\zeta|^2 + |A_{12}\cos\zeta + A_{22}\sin\zeta|^2}}{|M|},$$

and the sensitivity is given by the ratio of the noise and the signal components at this readout quadrature. Coefficient M represents the amplification factor of the optical spring. As explained in Buonanno and Chen's paper [15], the roots of the equation $M = 0$ provide the optical spring and optical resonance frequencies, at which the quantum noise sensitivity spectrum can be improved.

The optical resonance is approximately given by

$$\Omega_{\rm res} \simeq \frac{c}{L}\sqrt{\frac{1}{2} - \frac{1}{4}\left(s + \frac{1}{s}\right)\cos 2\phi}. \tag{7}$$

By defining

$$\phi_s \equiv \frac{1}{2}\arccos\left[\frac{1}{2}\left(s + \frac{1}{s}\right)\cos 2\phi\right] \tag{8}$$

the optical resonance can be expressed as $\Omega_{\rm res} \sim \phi_s c/L$, which becomes $\phi c/L$ without the parametric amplification. The expression coincides to that shown in Harms's paper [31].

Solving $M = 0$ with $\beta \to 0$, we obtain the optical spring frequency $\Omega_{\rm os}$ as follows:

$$\Omega_{\rm os} \simeq \sqrt{\frac{2\omega_0 I_{\rm BS}}{mc^2}\frac{(s+\frac{1}{s})\sin 2\phi - (s-\frac{1}{s})\sin(2\phi+2\eta)}{(r_s+\frac{1}{r_s}) - (s+\frac{1}{s})\cos 2\phi}}, \tag{9}$$

which can be maximized by choosing η to satisfy $\phi + \eta = \pi/4$ for $s < 1$ and $\phi + \eta = -\pi/4$ for $s > 1$ to obtain

$$\Omega_{\rm os}^{\rm opt} \simeq \sqrt{\frac{2\omega_0 I_{\rm BS}}{mc^2}\frac{(s+\frac{1}{s})\sin 2\phi + |s-\frac{1}{s}|}{(r_s+\frac{1}{r_s}) - (s+\frac{1}{s})\cos 2\phi}}. \tag{10}$$

Without the parametric amplification, the optical spring frequency appears infinitely high with $r \to 1$ and $\phi \to 0$, but intracavity optical losses limit it in reality. With parametric amplification, the optical spring frequency can be made significantly high by tuning the squeeze factor s even if r is limited to a decent value.

In fact, the optical resonance changes with s. We shall fix the optical resonance and compare the optical spring frequency with different parametric gain s. Define the detune phase at $s = 1$ as ϕ_0. The same optical resonance is given with the parametric amplification when $\phi_s = \phi_0$ is satisfied, that is, when the detuned phase ϕ is fixed to

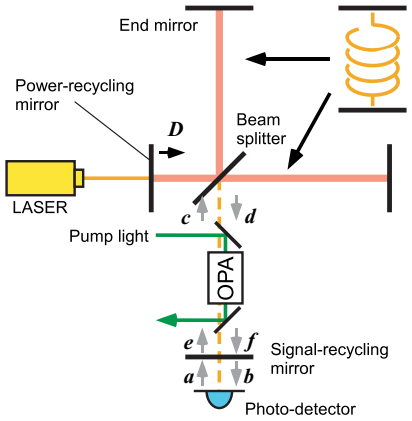

FIG. 1. Optical setup of the interferometer with an intracavity signal amplifier.

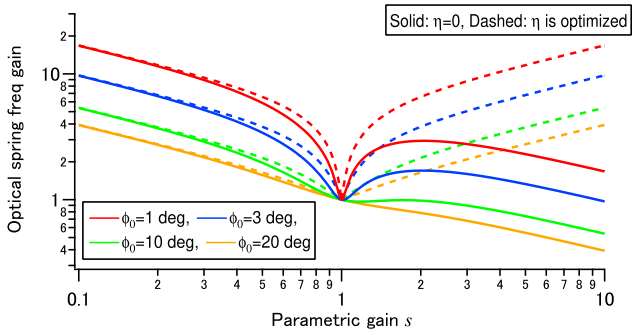

FIG. 2. The increasing rate of the optical spring frequency as a function of the parametric gain s.

$$\phi_{\rm fix} = \frac{1}{2}\arccos\left[\frac{2s}{1+s^2}\cos 2\phi_0\right]. \tag{11}$$

One can see that the detune phase approaches to $\pi/4$ when s moves away from unity. The increasing rate of the optical spring frequency by the parametric gain, defined by the ratio of $\Omega_{\rm os}(s,\phi_{\rm fix})$ to $\Omega_{\rm os}(s=1,\phi=\phi_0)$, is then calculated as

$$\left[\frac{(s-\frac{1}{s})^2+4\sin^2 2\phi_0}{(1+s^2)^2\sin^2 2\phi_0}\right]^{\frac{1}{4}}, \tag{12}$$

with η fixed to 0, and is given by

$$\left[\frac{\sqrt{(s-\frac{1}{s})^2+4\sin^2 2\phi_0}+|s-\frac{1}{s}|}{2\sin 2\phi_0}\right]^{\frac{1}{2}}, \tag{13}$$

with $\phi+\eta$ fixed to $\pi/4$ for $s<1$ and to $-\pi/4$ for $s>1$. Figure 2 illustrates the increasing rate of the optical spring frequency. The solid curves correspond to $\eta=0$ and the dashed curves correspond to η chosen to maximize the optical spring frequency. The denominator in Eq. (9) approaching to zero explains the steep increase of the increasing rate in the vicinity of $s=1$. Optimization of the squeeze angle makes the dashed curve symmetric for s and $1/s$. The optical spring frequencies $\Omega_{\rm os}^{\rm zero}$ and $\Omega_{\rm os}^{\rm max}$ coincide at $s\ll 1$, and one can assume $\eta\simeq 0$ for simplicity of the calculation. (See Khalili's work [32] for further discussion of η.)

III. SIGNAL RESPONSE FUNCTION AND QUANTUM-NOISE LIMITED SENSITIVITY

Figure 3 shows the signal response (top), noise response (middle), and quantum-noise limited sensitivity (bottom) of a detuned interferometer with and without the parametric amplifier for different signal-recycling mirror reflectivities. The response functions are dimensionless (see Sec. II for the definition) and the sensitivity is given by the power spectrum density of the vacuum field at the dark port multiplied by the ratio of the response functions. The laser power is 100 kW at the beam splitter, the test mass is 1 kg, the arm length is 1200 m, and the amplitude reflectivities of the signal recycling mirror are $\sqrt{0.99}$ for the left six panels and $\sqrt{0.9995}$ for the right six panels. The detune angle is set to $\phi_{\rm fix}$ in Eq. (11) with $\phi_0=5.74$ deg, which leads to an optical resonance frequency at 4 kHz; the condition does not depend much on r_s, and ϕ_0 is nearly equal for $r_s=\sqrt{0.99}$ and $r_s=\sqrt{0.9995}$. For simplicity, the squeeze angle rotation η is fixed to zero. Different colors represent different parametric gains ($s=1, 1/2, 1/10, 1/70, 1/500$ for red, blue, green, orange, and purple, respectively). The readout phase ζ is fixed to zero for the results in the left column of each 6-panel block and tuned to improve the sensitivity for the results in the right column of the block. Let us first examine the results without amplification (red curves). The noise source comprises a vacuum field directly reflected by the signal-recycling mirror and a vacuum field that emerges from the interferometer. The former is flat in frequency and the latter is amplified around the optical spring frequency. The signal is also amplified by the optical spring, and the gain is higher than the noise response owing to the presence of a directly reflected vacuum field. Thus, the sensitivity is improved around the optical spring.

The leftmost column of Fig. 3 shows that the peak of the optical spring moves to a higher frequency with parametric gain but the dip at the optical spring frequency vanishes in the sensitivity. This can be explained by the fact that the noise response also increases with parametric gain. Owing to the significant active amplification of the fields inside the SRC, the contribution of a vacuum field directly reflected by the signal recycling mirror becomes negligible.

There are two approaches to improve the sensitivity with making use of the amplified optical spring. One is to

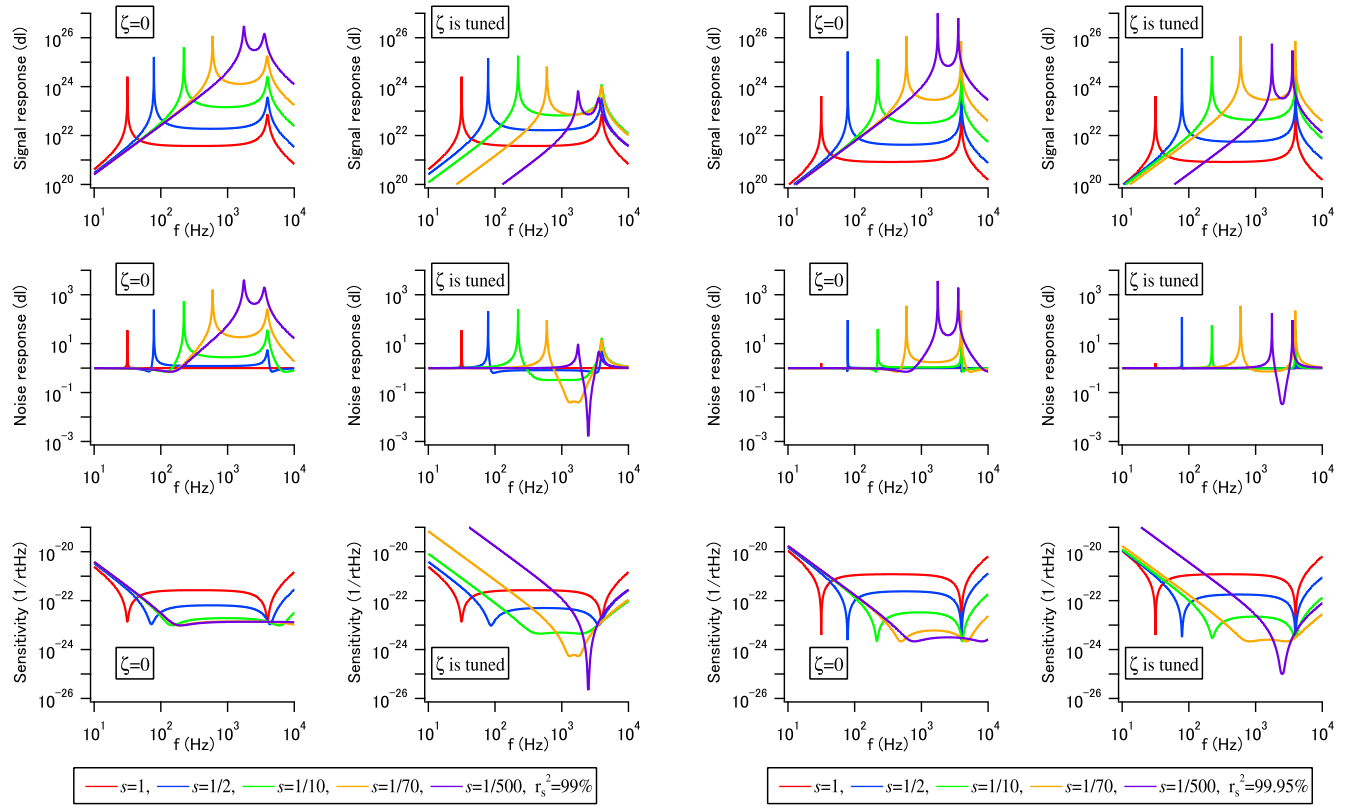

FIG. 3. The frequency responses of signal (top) and noise (middle), and the quantum-noise limited sensitivity (bottom) of a detuned signal-recycling interferometer with the parametric amplifier; dl stands for dimensionless. The readout phase is fixed to zero in the left column and is tuned to improve the sensitivity in the right column. The optical losses are not included.

increase the reflectivity of the signal recycling mirror. The second right column of Fig. 3 presents the optical spring in the sensitivity more clearly and the noise level is lower at 2–3 kHz compared with that of the leftmost column. The other approach is to tune the readout phase. In the second left column of Fig. 3, the readout phase ζ is selected to be 85 deg for $s = 1/2$, 64 deg for $s = 1/10$, 47.25 deg for $s = 1/70$, and 45.0947 deg for $s = 1/500$. In the rightmost column of Fig. 3, the readout phase ζ is selected to be 120 deg for $s = 1/2$ and $s = 1/10$, 90 deg for $s = 1/70$, and 46.9 deg for $s = 1/500$. Both the signal and noise responses decrease in a certain frequency band, and the sensitivity can reach a level of $10^{-24}(1/\sqrt{\mathrm{Hz}})$ in strain. The noise field is highly squeezed in the frequency band between the optical spring and optical resonance frequencies. However, this approach is highly sensitive to the optical losses discussed in the following section.

IV. OPTICAL LOSSES OF THE INTRACAVITY SYSTEM

In this section, we introduce optical losses in the mathematical expression according to the calculation by Yaginuma [33]. Here the squeeze angle rotation η is fixed to zero for simplicity. The input-output relations of the fields are given as

$$\begin{aligned}
\boldsymbol{b} &= \sqrt{1-\epsilon_{\mathrm{PD}}}(-r_s\boldsymbol{a} + t_s\boldsymbol{f}) + \sqrt{\epsilon_{\mathrm{PD}}}\boldsymbol{u},\\
\boldsymbol{e} &= \sqrt{1-\epsilon_{\mathrm{SR}}}(r_s\boldsymbol{f} + t_s\boldsymbol{a}) + \sqrt{\epsilon_{\mathrm{SR}}}\boldsymbol{v},\\
\boldsymbol{c} &= \mathbb{R}(\phi)\boldsymbol{e}, \qquad \boldsymbol{f} = \mathbb{R}(\phi)\mathbb{S}(s,0)\boldsymbol{d},\\
\boldsymbol{d} &= \mathbb{K}\boldsymbol{c}e^{2i\beta} + \alpha\boldsymbol{h}e^{i\beta},
\end{aligned} \tag{14}$$

where ϵ_{PD} and ϵ_{SR} are the optical losses at the photo detection and optical losses in the SRC, respectively, and $\boldsymbol{u}$ and $\boldsymbol{v}$ are the loss vacuums introduced at the photo detection and SRC, respectively. The optical losses of the end mirrors, the nonlinear crystal, and the beam splitter are included in the loss in the SRC, as the frequency responses are all identical. Solving the series of equations, we obtain

$$\boldsymbol{b} = \frac{1}{M^{\mathrm{L}}}(\mathbb{A}^{\mathrm{L}}\boldsymbol{a}e^{2i\beta} + \mathbb{H}^{\mathrm{L}}\boldsymbol{h}e^{i\beta} + \mathbb{U}\boldsymbol{u} + \mathbb{V}\boldsymbol{v}e^{2i\beta}), \tag{15}$$

with

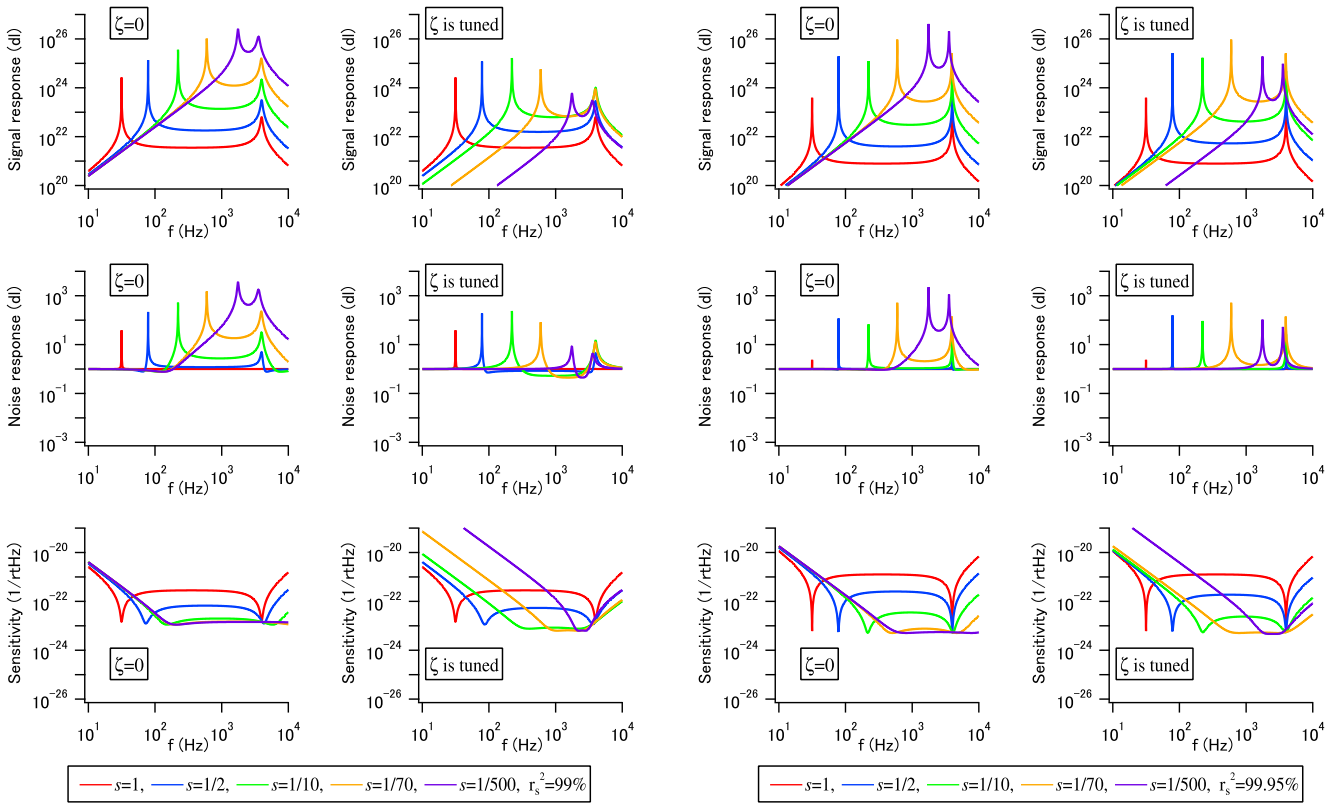

FIG. 4. The frequency responses of signal (top) and noise (middle), and the quantum-noise limited sensitivity (bottom) of a detuned signal-recycling interferometer with the parametric amplifier; dl stands for dimensionless. The readout phase is fixed to zero in the left column and is tuned to improve the sensitivity in the right column. The optical losses (1000 ppm in the SRC and 10% at the photo detection) are included.

$$
\begin{aligned}
M^{\mathrm{L}} &= s + s r_s^2 (1-\epsilon_{\mathrm{SR}}) e^{4i\beta} \\
&\quad - r_s \sqrt{1-\epsilon_{\mathrm{SR}}} e^{2i\beta} [(1+s^2)\cos 2\phi + \mathcal{K} \sin 2\phi], \\
A_{11}^{\mathrm{L}} &= \sqrt{1-\epsilon_{\mathrm{PD}}-\epsilon_{\mathrm{SR}}} \left[-\frac{1-s^2}{2} t_s^2 \right. \\
&\quad \left. + (1+r_s^2) \left(\frac{1+s^2}{2} \cos 2\phi + \frac{\mathcal{K}}{2} \sin 2\phi \right) \right] \\
&\quad - s r_s \left(\sqrt{1-\epsilon_{\mathrm{PD}}} e^{-2i\beta} + \sqrt{1-\epsilon_{\mathrm{PD}}-2\epsilon_{\mathrm{SR}}} e^{2i\beta} \right), \\
A_{12}^{\mathrm{L}} &= -\sqrt{1-\epsilon_{\mathrm{PD}}-\epsilon_{\mathrm{SR}}} t_s^2 \left(\frac{1+s^2}{2} \sin 2\phi + \mathcal{K} \sin^2 \phi \right), \\
A_{21}^{\mathrm{L}} &= \sqrt{1-\epsilon_{\mathrm{PD}}-\epsilon_{\mathrm{SR}}} t_s^2 \left(\frac{1+s^2}{2} \sin 2\phi - \mathcal{K} \cos^2 \phi \right), \\
A_{22}^{\mathrm{L}} &= \sqrt{1-\epsilon_{\mathrm{PD}}-\epsilon_{\mathrm{SR}}} \left[\frac{1-s^2}{2} t_s^2 \right. \\
&\quad \left. + (1+r_s^2) \left(\frac{1+s^2}{2} \cos 2\phi + \frac{\mathcal{K}}{2} \sin 2\phi \right) \right] \\
&\quad - s r_s \left(\sqrt{1-\epsilon_{\mathrm{PD}}} e^{-2i\beta} + \sqrt{1-\epsilon_{\mathrm{PD}}-2\epsilon_{\mathrm{SR}}} e^{2i\beta} \right), \\
H_{12}^{\mathrm{L}} &= -t_s \alpha \left(\sqrt{1-\epsilon_{\mathrm{PD}}-\epsilon_{\mathrm{SR}}} \right. \\
&\quad \left. + \sqrt{1-\epsilon_{\mathrm{SR}}-2\epsilon_{\mathrm{SR}}} s r_s e^{2i\beta} \right) \sin \phi, \\
H_{22}^{\mathrm{L}} &= t_s \alpha \left(\sqrt{1-\epsilon_{\mathrm{PD}}-\epsilon_{\mathrm{SR}}} \right. \\
&\quad \left. - \sqrt{1-\epsilon_{\mathrm{SR}}-2\epsilon_{\mathrm{SR}}} s r_s e^{2i\beta} \right) \cos \phi, \\
H_{11}^{\mathrm{L}} &= H_{21}^{\mathrm{L}} = 0, \\
V_{11} &= \sqrt{\epsilon_{\mathrm{SR}}} t_s \left(\frac{1+s^2}{2} \cos 2\phi + \frac{\mathcal{K}}{2} \sin 2\phi - s r_s e^{2i\beta} - \frac{1-s^2}{2} \right), \\
V_{12} &= -\sqrt{\epsilon_{\mathrm{SR}}} t_s \left(\frac{1+s^2}{2} \sin 2\phi + \mathcal{K} \sin^2 \phi \right), \\
V_{21} &= \sqrt{\epsilon_{\mathrm{SR}}} t_s \left(\frac{1+s^2}{2} \sin 2\phi - \mathcal{K} \cos^2 \phi \right), \\
V_{22} &= \sqrt{\epsilon_{\mathrm{SR}}} t_s \left(\frac{1+s^2}{2} \cos 2\phi + \frac{\mathcal{K}}{2} \sin 2\phi - s r_s e^{2i\beta} + \frac{1-s^2}{2} \right), \\
U_{11} &= U_{22} = \sqrt{\epsilon_{\mathrm{PD}}} M^{\mathrm{L}}, \\
U_{12} &= U_{21} = 0.
\end{aligned}
\tag{16}
$$

Here, we ignore higher-order terms of ϵ_{PD} and ϵ_{SR}. The signal response function is given by $|(H_{12}^{\mathrm{L}} \cos\zeta + H_{22}^{\mathrm{L}} \sin\zeta)/M^{\mathrm{L}}|$, the noise response function is given by

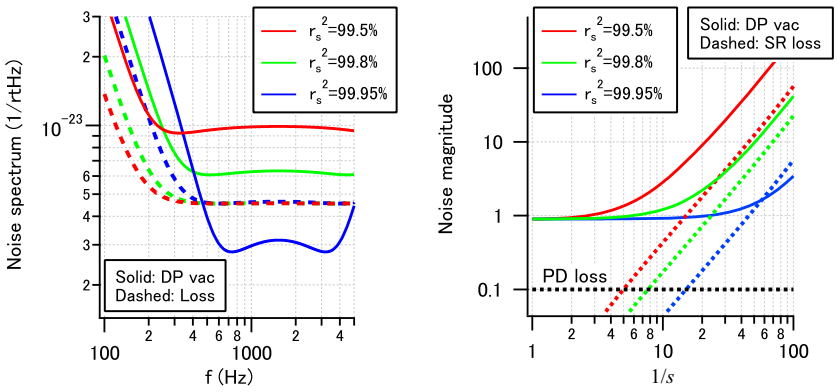

FIG. 5. Left: contributions of the dark port (DP) vacuum and the loss fields with different signal recycling mirror reflectivities. The parametric gain is $s = 1/70$ and the readout phase is chosen to flatten the noise floor for each curve. Right: magnitudes of the DP vacuum field and the loss fields emerging from the interferometer regarding the inverse of the parametric gain s. The noise magnitude is the area of the noise ellipse shown in Appendix A.

$$\frac{1}{|M^{\mathrm{L}}|}\Big[|A^{\mathrm{L}}_{11}\cos\zeta + A^{\mathrm{L}}_{21}\sin\zeta|^2 + |A^{\mathrm{L}}_{12}\cos\zeta + A^{\mathrm{L}}_{22}\sin\zeta|^2 + |V_{11}\cos\zeta + V_{21}\sin\zeta|^2 + |V_{12}\cos\zeta + V_{22}\sin\zeta|^2 + |U_{11}\cos\zeta + U_{21}\sin\zeta|^2 + |U_{12}\cos\zeta + U_{22}\sin\zeta|^2\Big]^{\frac{1}{2}},$$

and the sensitivity is given by the ratio of the noise and the signal components at ζ. Figure 4 shows the signal response (top), the noise response (middle), and the quantum-noise limited sensitivity (bottom) with the same interferometer setup as that used in Fig. 3 but with optical losses $\epsilon_{\mathrm{SR}} = 1000$ ppm and $\epsilon_{\mathrm{PD}} = 10\%$. Note that the noise response function is the root sum square of responses of dark port vacuum and all the loss fields. Compared with the results shown in Fig. 3, the noise response does not go much beyond the level of the vacuum fluctuation at frequencies between the optical spring and optical resonance for $r_s = \sqrt{0.99}$ and does not reach the level for $r_s = \sqrt{0.9995}$. The signal response decreases with loss, but the difference from the lossless case is trivial. The approach to improve the sensitivity by fine-tuning the readout phase turns out to be not as effective in the presence of optical losses. On the other hand, the other approach to improve the sensitivity by employing a high reflectivity signal-recycling mirror remains effective. The left panel of Fig. 5 shows the contributions of the vacuum field entering the interferometer through the dark port ($\boldsymbol{a}$) and the loss fields ($\boldsymbol{v}$ and $\boldsymbol{u}$) with different r_s. The parametric gain is $s = 1/70$, the detune phase is set to ϕ_{fix} for each curve, and the readout phases are chosen to flatten the dark port vacuum contributions on the floor; -28.6 deg, -45.8 deg, -68.8 deg for $r_s^2 = 99.5, 99.8, 99.95\%$, respectively. While the dark port vacuum contribution decreases with a high signal-recycling mirror reflectivity, the loss contribution does not depend much on the reflectivity. The right panel of Fig. 5 shows the magnitudes of the noise fields given by the determinant of the matrices multiplied to the fields in Eq. (15). Both the dark port vacuum and the intracavity loss field are not only squeezed but magnified by the intracavity parametric amplifier. The internal loss behavior is explained in Appendix A.

V. TARGET SENSITIVITY

Figure 6 shows the target sensitivity obtained using an intracavity parametric amplifier. The parameters used to calculate the sensitivity are same as those used for the orange curve in the second right panel of Fig. 4: $s = 1/70$, $r_s = \sqrt{0.9995}$, $\zeta = 0$, $m = 1$ kg, and $I_{\mathrm{BS}} = 100$ kW. The loss contribution is dominant in the sensitivity. The signal recycling mirror reflectivity is chosen to reduce the influence of dark port vacuum contribution while maintaining the floor bandwidth as high as 3 kHz. We show three sensitivity curves, Advanced LIGO, KAGRA, and Einstein Telescope, as references. It should be noted that our target sensitivity does not include classical noise. The target sensitivity is better than that of the second generation detectors by some factors in the frequency band of 1–3 kHz.

The sensitivity could reach $10^{-24}(1/\sqrt{\mathrm{Hz}})$ at 1–3 kHz with more ambitious parameters: $s = 1/200$, $r_s = \sqrt{0.9999}$, $\epsilon_{\mathrm{SR}} = 100$ ppm, $m = 5$ kg, and $I_{\mathrm{BS}} = 300$ kW ($\zeta = 80.2$ deg, $\phi = 44.1962$ deg). The noise level is comparable to the sensitivity of Einstein Telescope in the frequency band, and it satisfies the requirement of observing the postmerger remnant of a binary neutron star collision with sufficient regularity, which is suggested in the study of NEMO [4]. Almost the same sensitivity can be realized with a decent requirement for the internal loss if the arm length is increased to 4 km; the parameters are as follows: $s = 1/200$, $r_s = \sqrt{0.999}$, $\epsilon_{\mathrm{SR}} = 1000$ ppm, $m = 0.5$ kg, and $I_{\mathrm{BS}} = 300$ kW ($\zeta = 0$,

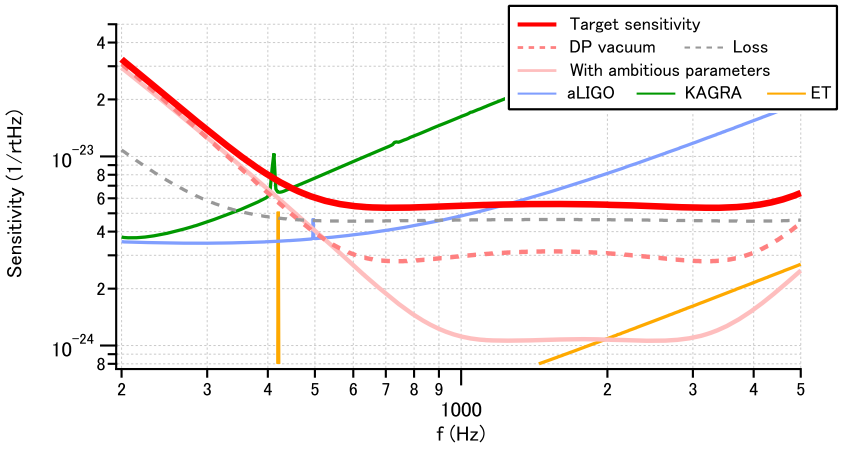

FIG. 6. Quantum-noise limited sensitivity with the intracavity parametric amplifier. The parameters used for the target sensitivity are mostly the same as those used for the orange curve in the second right panel of Fig. 4: $s = 1/70$, $r_s = \sqrt{0.9995}$, $\zeta = 0$, $m = 1$ kg, and $I_{\mathrm{BS}} = 100$ kW. The detune phase is slightly shifted from ϕ_{fix} (by 0.017 deg) to flatten the noise floor. Sensitivity curves of Advanced LIGO (aLIGO), KAGRA, and Einstein Telescope (ET) are shown as references. We also plot a sensitivity curve with more ambitious parameters, which reaches $10^{-24}(1/\sqrt{\mathrm{Hz}})$.

$\phi = 44.7336$ deg). See Appendix B for a discussion of the arm length.

VI. SUMMARY AND FUTURE PROSPECTS

We presented the intracavity signal amplification technique, one of the most promising techniques for next-generation gravitational wave detectors to observe sources in the kilohertz band. The quantum-noise limited strain sensitivity can go beyond the sensitivity of second-generation detectors and can even reach $10^{-24}(1/\sqrt{\mathrm{Hz}})$ with somewhat ambitious parameters. Our study revealed that the noise field could be magnified with intracavity amplifier in the presence of internal optical loss. This interesting behavior of the internal loss can easily limit the sensitivity; therefore the interferometer parameters should be carefully chosen.

In this work, the squeeze angle rotation η is fixed to zero or chosen to maximize the optical spring frequency. It is because the purpose of the intracavity amplifier has been to increase the optical spring frequency to a few kilohertz. Choosing a different η, one can certainly improve the sensitivity at different frequencies with the optical spring. It would be thus an interesting option to consider frequency dependent η to possibly improve the sensitivity in a broad frequency band. This approach is analogous to the frequency dependent squeezing technique [9] that has been implemented in the current gravitational-wave detectors [34,35].

In parallel with the theoretical efforts to further improve the sensitivity curve, it is essential to experimentally demonstrate the effectiveness of the technique. Prototype experiments have been conducted in multiple institutes. Researchers at the University of Western Australia employed a thin membrane as the test mass and observed the optical spring with a single optical resonator and an intracavity parametric amplifier [36]. Otabe *et al.* observed the optical spring with a single resonator and an intracavity amplifier but found the second harmonics generation of the carrier light prevents the optical system for approaching the threshold of the decent amplification of the signal field [37]. Harada *et al.* succeeded in operating the signal recycling interferometer with an intracavity parametric amplifier, attempting to observe the shift of the optical spring frequency [38,39].

ACKNOWLEDGMENTS

This work was supported by JST CREST (JPMJCR1873), JSPS Kakenhi (24684014), Grant-in-Aid for JSPS Fellows (20J22778), and Sumitomo Foundation (200629). We would like to thank our former colleagues for supporting the project: J. Kato, K. Yano, Y. Kataoka, T. Yaginuma, and K. Kusayanagi. We would also like to thank Y. Michimura and K. Komori for valuable discussions. We would like to thank Editage [40] for editing and reviewing the manuscript for English language.

APPENDIX A: OPTICAL LOSSES WITH THE INTRACAVITY AMPLIFIER

In Fig. 5, we observe that the noise field magnitude can be larger than the magnitude of the input field. This interesting phenomena cannot be observed in the case without an intracavity amplifier. The top panel of Fig. 7 shows the simple experimental setup of a single optical resonator and intracavity amplifier. The vacuum field $\boldsymbol{a}$ is injected from the left side through the input mirror with amplitude reflectivity $r_1 = \sqrt{0.99}$ and amplitude transmittance $t_1 = \sqrt{0.01}$. The loss vacuum $\boldsymbol{c}$ is injected from

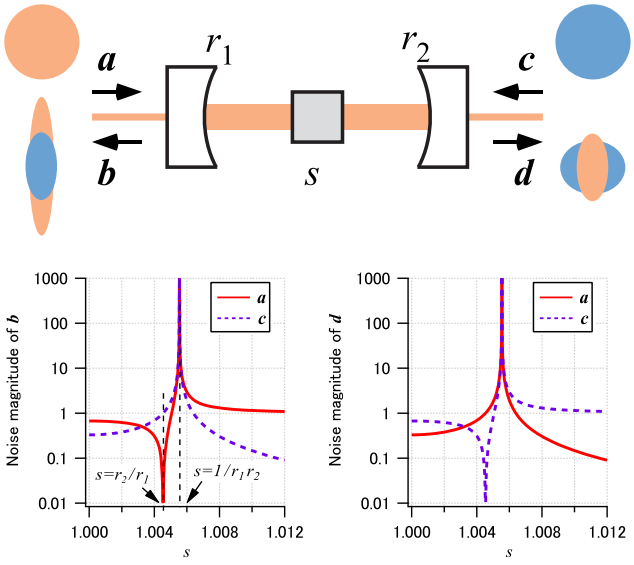

FIG. 7. Top: Vacuum field $\boldsymbol{a}$ (red circle) injected to a single optical resonator through the input mirror with the amplitude reflectivity of r_1 and the loss field $\boldsymbol{c}$ (blue circle) injected through the end mirror with the amplitude reflectivity of r_2. The output fields $\boldsymbol{b}$ and $\boldsymbol{d}$ comprise of $\boldsymbol{a}$ (red ellipses) and $\boldsymbol{c}$ (blue ellipses), both of which are squeezed by the intracavity parametric amplifier. Bottom: magnitudes of the output fields as a function of the parametric gain s. Below the threshold $s = r_2/r_1$, the squared sum of the magnitudes of each input field (either red or purple in two plots) emerging from the two ports is kept in unity. Above the threshold, the output fields are larger than the input fields.

the other side through the end mirror with $r_2 = \sqrt{0.999}$ and $t_2 = \sqrt{0.001}$. The output fields are $\boldsymbol{b}$ on the left side and $\boldsymbol{d}$ on the right side. Actually, the $\boldsymbol{d}$ field is lost and it cannot be extracted in the end. Each output field comprises a fraction of $\boldsymbol{a}$ and $\boldsymbol{c}$, which are squeezed by the intracavity amplifier with gain s. The bottom panel of Fig. 7 shows the calculated noise magnitude of the contributing input fields for each output field. Here the noise magnitude is the area of the noise ellipse, which is given by the product of two quadrature components, $b_1 \times b_2$ for example, or mathematically by the determinant of the matrix multiplied by the field. Let us focus on field $\boldsymbol{a}$. A significant fraction of the field is reflected and a small fraction transmits through the resonator without the amplifier ($s = 1$). The noise magnitude is less than unity for either the reflected or transmitted field. With the amplifier (let us consider $s > 1$), the reflectivity and transmittance of the resonator are given by

$$r_{a_1} = \frac{-r_1 + r_2 s}{1 - r_1 r_2 s}, \qquad r_{a_2} = \frac{-r_1 s + r_2}{s - r_1 r_2},$$
$$t_{a_1} = \frac{t_1 t_2 s}{1 - r_1 r_2 s}, \qquad t_{a_2} = \frac{t_1 t_2}{s - r_1 r_2} \tag{A1}$$

for each quadrature component. The noise magnitude at the reflection becomes zero with $s = r_2/r_1 (\equiv s_{\rm th})$ and the noise magnitude both at the reflection and at the transmission becomes infinity with $s = 1/r_1 r_2$. Above the threshold, $s > s_{\rm th}$, the noise magnitude of the transmitted field exceeds unity, and that of the reflected field exceeds unity when s becomes larger than $1/r_2$. This irregular phenomenon may appear to violate the energy conservation law; however, the signs of the coefficients in front of the reflected and transmitted fields are the opposite. If we could coherently subtract the two fields with a certain combination, then the output fields must have the magnitude of unity, but this is impossible because the transmitted field is actually lost. The noise field ends up being increased by the resonator with an intracavity amplifier.

APPENDIX B: ARM LENGTH AND STRAIN SENSITIVITY

If the arm length is enlarged by a factor n, the detune phase shall be reduced by the same factor to maintain the same optical resonance. The parametric gain s' required to obtain the same optical spring frequency can be derived by solving Eq. (13) with ϕ_0 reduced by n or approximately with $\sin\phi_0$ reduced by n:

$$\frac{\sqrt{A^2 + 4\sin^2 2\phi_0} - A}{2\sin^2 2\phi_0} = \frac{\sqrt{A'^2 + 4\sin^2(2\phi_0/n)} - A'}{2\sin^2(2\phi_0/n)}, \tag{B1}$$

where we consider the inside of the square root of Eq. (13) and we define $A = s - 1/s$ and $A' = s' - 1/s'$. Equation (B1) can be reduced to the following form:

$$A' = \frac{1}{2}\left\{(1+\epsilon)A - \sqrt{(1-\epsilon)^2 A^2 - 4(1-\epsilon)}\right\}$$
$$\simeq \epsilon A (A \gg 1). \tag{B2}$$

Here, we define $\epsilon \equiv (\sin^2(2\phi_0/n)/\sin^2 2\phi_0)^2$, which can be approximated as $\simeq 1/n^2$ when the detune angle (without parametric amplification) is sufficiently small. Calculating the sensitivity, we can see that the noise level in displacement is identical with a different arm length in the lossless case.

[1] B. P. Abbott *et al.*, Observation of Gravitational Waves from a Binary Black Hole Merger, Phys. Rev. Lett. **116**, 061102 (2016).

[2] B. P. Abbott *et al.*, GW170817: Observation of Gravitational Waves from a Binary Neutron Star Inspiral, Phys. Rev. Lett. **119**, 161101 (2017).

[3] Nikhil Sarin and Paul D. Lasky, The evolution of binary neutron star post-merger remnants: A review, Gen. Relativ. Gravit. **53**, 59 (2021).

[4] K. Ackley, V. B. Adya, P. Agrawal, P. Altin, G. Ashton, M. Bailes, E. Baltinas, A. Barbuio, D. Beniwal, C. Blair *et al.*, Neutron star extreme matter observatory: A kilohertz-band gravitational-wave detector in the global network, Pub. Astron. Soc. Aust. **37**, e047 (2020).

[5] Kentaro Somiya, Detector configuration of KAGRA–the Japanese cryogenic gravitational-wave detector, Classical Quantum Gravity **29**, 124007 (2012).

[6] Yuta Michimura *et al.*, Prospects for improving the sensitivity of the cryogenic gravitational wave detector KAGRA, Phys. Rev. D **102**, 022008 (2020).

[7] M Punturo *et al.*, The Einstein telescope: A third-generation gravitational wave observatory, Classical Quantum Gravity **27**, 194002 (2010).

[8] B P Abbott *et al.*, Exploring the sensitivity of next generation gravitational wave detectors, Classical Quantum Gravity **34**, 044001 (2017).

[9] H. J. Kimble, Yuri Levin, Andrey B. Matsko, Kip S. Thorne, and Sergey P. Vyatchanin, Conversion of conventional gravitational-wave interferometers into quantum nondemolition interferometers by modifying their input and/or output optics, Phys. Rev. D **65**, 022002 (2001).

[10] J. Abadie *et al.*, A gravitational wave observatory operating beyond the quantum shot-noise limit, Nat. Phys. **7**, 962 (2011).

[11] F. Acernese *et al.*, Increasing the Astrophysical Reach of the Advanced Virgo Detector via the Application of Squeezed Vacuum States of Light, Phys. Rev. Lett. **123**, 231108 (2019).

[12] M. Tse *et al.*, Quantum-Enhanced Advanced LIGO Detectors in the Era of Gravitational-Wave Astronomy, Phys. Rev. Lett. **123**, 231107 (2019).

[13] Alessandra Buonanno and Yanbei Chen, Quantum noise in second generation, signal-recycled laser interferometric gravitational-wave detectors, Phys. Rev. D **64**, 042006 (2001).

[14] Denis Martynov, Haixing Miao, Huan Yang, Francisco Hernandez Vivanco, Eric Thrane, Rory Smith, Paul Lasky, William E. East, Rana Adhikari, Andreas Bauswein, Aidan Brooks, Yanbei Chen, Thomas Corbitt, Andreas Freise, Hartmut Grote, Yuri Levin, Chunnong Zhao, and Alberto Vecchio, Exploring the sensitivity of gravitational wave detectors to neutron star physics, Phys. Rev. D **99**, 102004 (2019).

[15] Alessandra Buonanno and Yanbei Chen, Signal recycled laser-interferometer gravitational-wave detectors as optical springs, Phys. Rev. D **65**, 042001 (2002).

[16] J. Mizuno, Comparison of optical configurations for laser-interferometric gravitational-wave detectors, Ph.D. thesis, University of Hannover, 1995.

[17] V. B. Braginsky, M. L. Gorodetsky, and F. Ya. Khalili, Optical bars in gravitational wave antennas, Phys. Lett. A **232**, 340 (1997).

[18] F. Ya. Khalili, The "optical lever" intracavity readout scheme for gravitational-wave antennae, Phys. Lett. A **298**, 308 (2002).

[19] K. Somiya and Y. Chen, Ponderomotive amplifier to reduce shot noise, LIGO-G1000568-v1, GWADW, Kyoto, 2010.

[20] Kentaro Somiya, Shinichiro Ueda, and Yuki Susa, Intracavity squeezing for a gravitational-wave detector, JGW-T1215017-v1, internal report (2012).

[21] K. Somiya, Y. Kataoka, J. Kato, N. Saito, and K. Yano, Parametric signal amplification to create a stiff optical bar, Phys. Lett. A **380**, 521 (2016).

[22] V. B. Adya, M. J. Yap, D. Töyrä, T. G. McRae, P. A. Altin, L. K. Sarre, M. Meijerink, N. Kijbunchoo, B. J. J. Slagmolen, R. L. Ward, and D. E. McClelland, Quantum enhanced kHz gravitational wave detector with internal squeezing, Classical Quantum Gravity **37**, 07LT02 (2020).

[23] Mikhail Korobko, Yiqiu Ma, Yanbei Chen, and Roman Schnabel, Quantum expander for gravitational-wave observatories, Light **8**, 118 (2019).

[24] Haixing Miao, Yiqiu Ma, Chunnong Zhao, and Yanbei Chen, Enhancing the Bandwidth of Gravitational-Wave Detectors with Unstable Optomechanical Filters, Phys. Rev. Lett. **115**, 211104 (2015).

[25] Xiang Li, Maxim Goryachev, Yiqiu Ma, Michael E. Tobar, Chunnong Zhao, Rana X. Adhikari, and Yanbei Chen, Broadband sensitivity improvement via coherent quantum feedback with pt symmetry, arXiv:2012.00836.

[26] Xiang Li, Jiri Smetana, Amit Singh Ubhi, Joe Bentley, Yanbei Chen, Yiqiu Ma, Haixing Miao, and Denis Martynov, Enhancing interferometer sensitivity without sacrificing bandwidth and stability: Beyond single-mode and resolved-sideband approximation, Phys. Rev. D **103**, 122001 (2021).

[27] Chuming Wang, Chunnong Zhao, Xiang Li, Enping Zhou, Haixing Miao, Yanbei Chen, and Yiqiu Ma, Boosting the sensitivity of high-frequency gravitational wave detectors using pt-symmetry, Phys. Rev. D **106**, 082002 (2022).

[28] Haixing Miao, Huan Yang, and Denis Martynov, Towards the design of gravitational-wave detectors for probing neutron-star physics, Phys. Rev. D **98**, 044044 (2018).

[29] B Willke *et al.*, The GEO 600 gravitational wave detector, Classical Quantum Gravity **19**, 1377 (2002).

[30] Carlton M. Caves and Bonny L. Schumaker, New formalism for two-photon quantum optics. I. Quadrature phases and squeezed states, Phys. Rev. A **31**, 3068 (1985).

[31] Jan Harms, Yanbei Chen, Simon Chelkowski, Alexander Franzen, Henning Vahlbruch, Karsten Danzmann, and Roman Schnabel, Squeezed-input, optical-spring, signal-recycled gravitational-wave detectors, Phys. Rev. D **68**, 042001 (2003).

[32] Mikhail Korobko, F. Ya. Khalili, and Roman Schnabel, Engineering the optical spring via intra-cavity optical-parametric amplification, Phys. Lett. A **382**, 2238 (2018).

[33] Takuya Yaginuma, Study of the gravitational-wave detector with an intracavity parametric amplifier and the behavior of the optical losses (in Japanese), Master thesis, Tokyo Institute of Technology, 2018.

[34] L. McCuller, C. Whittle, D. Ganapathy, K. Komori, M. Tse, A. Fernandez-Galiana, L. Barsotti, P. Fritschel, M. MacInnis, F. Matichard, K. Mason, N. Mavalvala, R. Mittleman, Haocun Yu, M. E. Zucker, and M. Evans, Frequency-Dependent Squeezing for Advanced LIGO, Phys. Rev. Lett. **124**, 171102 (2020).

[35] F. Acernese *et al.*, Frequency Dependent Squeezed Vacuum Source for the Advanced Virgo Gravitational-Wave detector, Phys. Rev. Lett. (to be published).

[36] Henxing Sun, Jue Zhang, Hui Guo, Michael Page, Xu Chen, Li Ju, Jiangrui Zhao, and Chunnong Zhao, Experimental demonstration of optical spring enhancement by an opto-mechanical parametric amplifier, LIGO-G2100568-v1, LVK March Meeting, Online (2021).

[37] Sotatsu Otabe, Photothermal and nonlinear optical effects in the signal amplification system for a gravitational wave detector, Doctor thesis, Tokyo Institute of Technology, 2023.

[38] Kaido Suzuki, Development of the signal amplification technique using a non-linear optical effect for the next-generation gravitational-wave detector (in Japanese), Master thesis, Tokyo Institute of Technology, 2023.

[39] Ken-ichi Harada, Kaido Suzuki, Sotatsu Otabe, and Kentaro Somiya, Development of signal amplification system using a non-linear optical effect for next-generation gravitational-wave detectors IX (in Japanese), 7aA122-11, JPS Meeting, Okayama (2022).

[40] http://www.editage.com.